

# Sub-5 nm hard x-ray point focusing by a combined Kirkpatrick-Baez mirror and multilayer zone plate

F. Döring,<sup>1</sup> A.L. Robisch,<sup>2</sup> C. Eberl,<sup>1</sup> M. Osterhoff,<sup>2</sup>  
A. Ruhlandt,<sup>2</sup> T. Liese,<sup>1</sup> F. Schlenkrich,<sup>1</sup> S. Hoffmann,<sup>2</sup>  
M. Bartels,<sup>2</sup> T. Salditt,<sup>2</sup> and H.U. Krebs<sup>1\*</sup>

<sup>1</sup>*Institut für Materialphysik, Universität Göttingen, Friedrich-Hund-Platz 1,  
37077 Göttingen, Germany*

<sup>2</sup>*Institut für Röntgenphysik, Universität Göttingen, Friedrich-Hund-Platz 1,  
37077 Göttingen, Germany*

[\\*krebs@ump.gwdg.de](mailto:krebs@ump.gwdg.de)

**Abstract:** Compound optics such as lens systems can overcome the limitations concerning resolution, efficiency, or aberrations which fabrication constraints would impose on any single optical element. In this work we demonstrate unprecedented sub-5 nm point focusing of hard x-rays, based on the combination of a high gain Kirkpatrick-Baez (KB) mirror system and a high resolution W/Si multilayer zone plate (MZIP) for ultra-short focal length  $f$ . The pre-focusing allows limiting the MZIP radius to below 2  $\mu\text{m}$ , compatible with the required 5 nm structure width and essentially unlimited aspect ratios, provided by enabling fabrication technology based on pulsed laser deposition (PLD) and focused ion beam (FIB).

© 2013 Optical Society of America

**OCIS codes:** (340.0340) X-ray optics; (220.0220) Optical design and fabrication.

---

## References and links

1. B. Niemann, D. Rudolph, and G. Schmahl, "Soft X-ray imaging zone plates with large zone numbers for microscopic and spectroscopic applications," *Opt. Commun.* **12**, 160–163 (1974).
2. C. Schroer, "Focusing hard x-rays to nanometer dimensions using Fresnel zone plates," *Phys. Rev. B* **74**, 033405 (2006).
3. H. Yan, J. Maser, A. Macrander, Q. Shen, S. Vogt, G.B. Stephenson, and H.C. Kang, "Takagi-Taupin description of x-ray dynamical diffraction from diffractive optics with large numerical aperture," *Phys. Rev. B* **76**, 115438 (2007).
4. A. Snigirev, V. Kohn, I. Snigireva, and B. Lengeler, "A compound refractive lens for focusing high-energy X-rays," *Nature* **384** 49–51 (1996).
5. C.G. Schroer, O. Kurapova, J. Patommel, P. Boye, J. Feldkamp, B. Lengeler, M. Burghammer, C. Riekel, L. Vincze, A. van der Hart, and M. Küchler, "Hard x-ray nanoprobe based on refractive x-ray lenses," *Appl. Phys. Lett.* **87**, 124103 (2005).
6. P. Kirkpatrick and A.V. Baez, "Formation of optical images by x-rays," *Opt. Soc. Am.* **38**, 766–773 (1948).
7. H. Mimura, S. Handa, T. Kimura, H. Yumoto, D. Yamakawa, H. Yokoyama, S. Matsuyama, K. Inagaki, K. Yamamura, Y. Sano, K. Tamasaku, Y. Nishino, M. Yabashi, T. Ishikawa, and K. Yamauchi, "Breaking the 10nm barrier in hard x-ray focusing," *Nature Phys.* **6**, 122 (2010).
8. K. Yamauchi, H. Mimura, T. Kimura, H. Yumoto, S. Handa, S. Matsuyama, K. Arima, Y. Sano, K. Yamamura, K. Inagaki, H. Nakamori, J. Kim, K. Tamasaku, Y. Nishino, M. Yabashi, and T. Ishikawa, "Single-nanometer focusing of hard x-rays by Kirkpatrick-Baez mirrors," *J. Phys.: Condensed Matter* **23**, 394206 (2011).
9. M. Howells, C. Jacobsen, T. Warwick, and A. Bos, "Principles and Applications of Zone Plate X-Ray Microscopes, in Hawkes," in *Science of Microscopy*, P. W., Spence, J. C. H., (Springer, New York, 2007), pp. 835–926.

10. J. Vila-Comamala, Y. Pan, J.J. Lombardo, W.M. Harris, W.K.S. Chiu, C. David, and Y. Wang, "Zone-doubled Fresnel zone plates for high-resolution hard X-ray full-field transmission microscopy," *J. Synchrotron Rad.* **19**, 705–709 (2012).
11. W. Chao, E. Anderson, G.P. Denbeaux, B. Harteneck, J.A. Liddle, D.L. Olynick, A.L. Pearson, F. Salmassi, C. Yu Song, and D.T. Attwood, "20-nm-resolution soft x-ray microscopy demonstrated by use of multilayer test structures," *Optics Lett.* **28**, 2019–2021 (2003).
12. K. Jefimovs, J. Vila-Comamala, T. Pilvi, J. Raabe, M. Ritala, and C. David, "Zone-Doubling Technique to Produce Ultrahigh-Resolution X-Ray Optics," *Phys. Rev. Lett.* **99**, 264801 (2007).
13. H.C. Kang, J. Maser, G.B. Stephenson, C. Liu, R. Conley, A.T. Macrander, and S. Vogt, "Nanometer Linear Focusing of Hard X-Rays by a Multilayer Laue Lens," *Phys. Rev. Lett.* **96**, 127401 (2006).
14. H.C. Kang, H. Yan, R.P. Winarski, M.V. Holt, J. Maser, C. Liu, R. Conley, S. Vogt, A.T. Macrander, and G.B. Stephenson, "Focusing of hard x-rays to 16 nanometers with a multilayer Laue lens," *Appl. Phys. Lett.* **92**, 221114 (2008).
15. A. Ruhlandt, T. Liese, V. Radisch, S.P. Krüger, M. Osterhoff, G. Giewekemeyer, H.U. Krebs, and T. Salditt, "A combined Kirkpatrick-Baez mirror and multilayer lens for sub-10nm x-ray focusing," *AIP Advances* **2**, 012175 (2012).
16. T. Koyama, T. Tsuji, H. Takano, Y. Kagoshima, S. Ichimaru, T. Ohchi, and H. Takenaka, "Development of Multilayer Laue Lenses; (2) Circular Type," *AIP Conf. Proc.: The 10th International Conference On X-Ray Microscope* **1365**, 100 (2011).
17. T. Koyama, H. Takano, S. Konishi, T. Tsuji, H. Takenaka, S. Ichimaru, T. Ohchi, and Y. Kagoshima, "Circular multilayer zone plate for high-energy x-ray nano-imaging," *Rev. Sci. Instrum.* **83**, 013705 (2012).
18. D. Attwood, *Soft X-rays and Extreme Ultraviolet Radiation* (Cambridge University Press, Cambridge, 1999).
19. M.J. Simpson and A.G. Michette, "Imaging properties of modified Fresnel zone plates," *Opt. Acta* **31**, 403–413 (1984).
20. D. Rudolph, B. Niemann, and G. Schmahl, *Proc. Soc. Photo-Opt. Instrum. Eng.* **316**, 103 (1981).
21. W.B. Yun, P.J. Viccaro, B. Lai, and J. Chrzas, "Coherent hard x-ray focusing optics and applications," *Rev. Sci. Instrum.* **63**, 582–585 (1992).
22. M. Yasumoto, S. Tamura, N. Kamijo, Y. Suzuki, A. Takeuchi, K. Uesugi, and Y. Terada, "Microstructure of Multilayer Fresnel Zone Plate for X-ray Focusing," *Physics Procedia* **32**, 157–160 (2012).
23. J. Röder, T. Liese, and H.U. Krebs, "Material-dependent smoothing of periodic rippled structures by pulsed laser deposition," *J. Appl. Phys.* **107**, 103515 (2010).
24. H.C. Kang, G.B. Stephenson, C. Liu, R. Conley, R. Khachatryan, M. Wiecek, A.T. Macrander, H. Yan, J. Maser, J. Hiller, and R. Koritala, "Sectioning of multilayers to make a multilayer Laue lens," *Rev. Sci. Instrum.* **78**, 046103 (2007).
25. T. Liese, V. Radisch, and H.U. Krebs, "Fabrication of multilayer Laue lenses by a combination of pulsed laser deposition and focused ion beam," *Rev. Sci. Instrum.* **81**, 073710 (2010).
26. H.U. Krebs and O. Bremert, "Pulsed laser deposition of thin metallic alloys," *Appl. Phys. Lett.* **62**, 2341–2343 (1993).
27. C. Eberl, T. Liese, F. Schlenkerich, F. Döring, H. Hofsäuss, and H.U. Krebs, "Enhanced resputtering and asymmetric interface mixing in W/Si multilayers," *Appl. Phys. A* **111**, 431–437 (2013).
28. J.W. Goodman, *J. Fourier Optics* (Roberts & Company Publishers, Greenwood Village, 2005).
29. H.M. Quiney, A.G. Peele, Z. Cai, D. Paterson, and K.A. Nugent, "Diffractive imaging of highly focused X-ray fields," *Nature Physics* **2**, 101–104 (2006).
30. C. Bergemann, H. Keymeulen, and J.F. van der Veen, "Focusing X-Ray Beams to Nanometer Dimensions," *Phys. Rev. Lett.* **91**, 204801 (2003).
31. D.G. Voelz and M.C. Roggemann, "Digital simulation of scalar optical diffraction: revisiting chirp function sampling criteria and consequences," *Appl. Opt.* **48**, 6132–6142 (2009).

## 1. Introduction

To date, x-ray focusing uses diffractive [1–3], refractive [4, 5] and reflective [6, 7] focusing elements, but has not yet sufficiently exploited the advantage of compound optics. Using an adaptive multilayer mirror system, already a focusing of 7 nm in one dimension (line focusing) was realized [7]. Also focusing in two dimensions could be achieved with focus sizes of 7 nm and 8 nm in horizontal and vertical direction, respectively [8]. However, the mirror system had been rotated for two individual measurements, and thus the determination of the focus was not instantaneous. Nowadays, most x-ray microscopes operate with diffractive optics, i.e. Fresnel zone plates (FZPs) fabricated by lithography, achieving two-dimensional (point) focusing even of hard x-rays with multi-keV photon energy [1, 2, 9], down to 17 nm [10]. However, con-

ventional FZPs are difficult to prepare with high aspect ratio [11] inevitably required for further progress in resolution, contrast and efficiency. The zone-doubling technique is one approach to enlarge aspect ratios in FZPs [12]. Alternatively, high aspect ratios are offered by diffractive optics fabricated by thin film deposition such as multilayer Laue lenses (MLL) [13–15] or multilayer zone plates (MZPs) [16, 17], which however, pose considerable fabrication challenges. MZPs are fabricated by depositing a depth graded multilayer according to the binary zone plate law on a rotating wire, with the position  $r_n$  of each zone  $n$  given by  $r_n = \sqrt{(n\lambda/2)^2 + n\lambda f}$  [18], with focal length  $f$  and wavelength  $\lambda$ . The focus spot size of the first diffraction order  $m = 1$  and hence the resolution depends on the outermost zone width according to  $\Delta \approx 1.22 dr$  with  $dr = r_n - r_{n-1}$ , but can even be somewhat smaller if the inner zones are blanked [19]. MZPs are usually fabricated by the sputter-slice technique [20, 21]. However, in most cases cumulative roughness of the multilayer occurs during sputter deposition on a curved wire spoiling the precise positioning of the outermost zones [22]. In contrast, during pulsed laser deposition (PLD) energetic particles with kinetic energies of up to 100 eV are deposited inducing high mobility and enhanced diffusion on the substrate surface. This results in a cumulative smoothening of roughness [23] and allows growing multilayers with both smooth and ultrathin layers. Additionally, the sputter-slice technique suffers of damaging the deposited multilayers during zone plate fabrication [24], which can be avoided by using focused ion beam (FIB) instead.

The benefit of using compound optics is illustrated by the fact that  $2 \cdot 10^4$  zones are needed for focusing with a single MZP to the same spot and aperture, as aperture sizes of more than hundred micrometers would be necessary to capture essential parts of the synchrotron beam. While  $10^3$  to  $10^4$  zones are possible to be fabricated by e-beam lithography, outermost zone widths of 5 nm can, to date, be exclusively achieved by thin film deposition, although stress and cumulative roughness imposes strong penalties for large devices. Hence the two-step focusing scheme seems to be indispensable. A further advantage is the higher possible bandwidth, since diffractive optics with a lower number of zones exhibit less dispersion, well matched to the essentially non-dispersive reflective optics.

Aim of this paper is to show that the PLD technique in combination with FIB allows to prepare a MZP with outermost layer width of about 5 nm. We will demonstrate that a compound optics consisting of a both high acceptance and high gain elliptical KB-mirror system with the MZP positioned nearby the focal plane of the KB mirror can be used for two-step hard x-ray nano-focusing down to less than 5 nm.

## 2. Design of the hard x-ray focusing experiment

Figure 1 shows the basic working principle of the hard x-ray point focusing experiment, which is similar to that recently used for line focusing down to 7 nm by a MLL [15]. First, a depth-graded multilayer was grown on a wire according to the zone plate law by PLD. Then, the MZP was fabricated by cutting a slice out of the multilayer with desired optical depth by FIB [25]. The MZP was positioned onto a W tip, which can be used as sample holder during hard x-ray focusing. The main idea of the x-ray focusing experiment was to place the fabricated MZP at the coherence beamline P10 of Petra III into an already prefocused x-ray beam slightly behind the focal plane and to use the lens for further nano-focusing. At this beamline, high intense prefocusing of the incoming x-ray beam down to a spot size of about  $400 \text{ nm} \times 200 \text{ nm}$  ( $h \times v$ ) is achieved using Kirkpatrick-Baez (KB) mirrors.

The MZP was designed for a wavelength  $\lambda$  of 0.157 nm and a focal length  $f$  of 50  $\mu\text{m}$ . The diameter of the central wire was 0.9  $\mu\text{m}$  (maximum deviation in local radius of curvature of 1.5 %) and layer thicknesses ranged between 8.6 nm and 5.0 nm. Starting with the 27th layer, 54 layers of W and Si were grown onto the rotating wire by PLD following the zone plate law.

In order to block the primary KB beam, a beamstop has been placed far behind the lens.

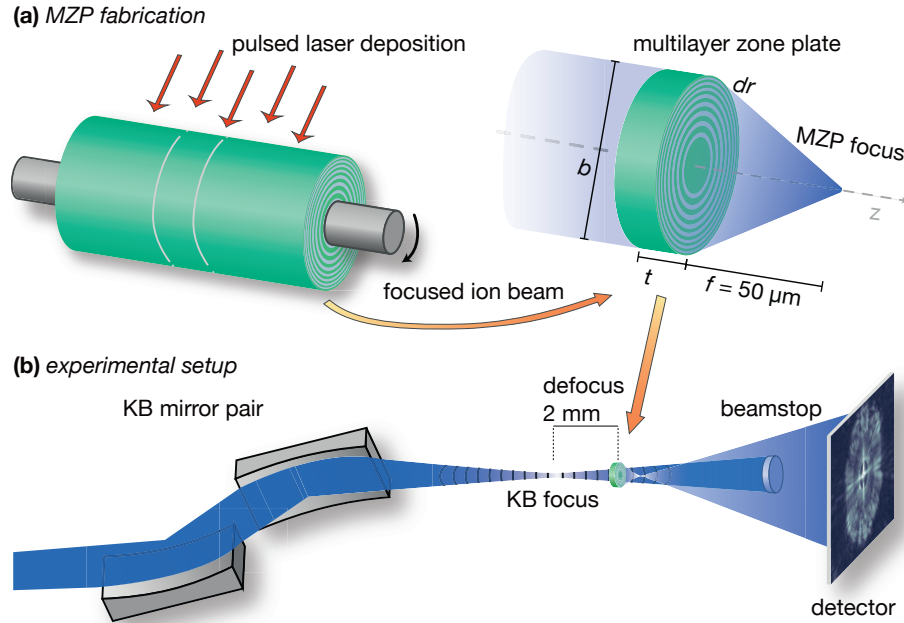


Fig. 1. (a) Schematic fabrication process: Pulsed laser deposition of W and Si multilayer onto a rotating wire according to the Fresnel zone plate law. Focused ion beam fabrication of the MZIP by cutting a slice out of the coated wire, placing it onto a sample holder and polishing it down to the optimal optical thickness of  $0.7 \mu\text{m}$ . (b) Experimental setup of the synchrotron experiment: The MZIP is positioned 2 mm downstream of the KB focus.

Compared to a single lens, this primary beam has a larger divergence due to the pre-focusing and thus beam stop alignment is easier. Also, since the beam is spread out among more pixels, single-photon counting detectors could be used improving the efficiency measurements. We would like to emphasize that the divergence of the diffracted beam is larger by one to two orders of magnitude, so the beamstop does not affect the MZIP far-field.

From the numerical multi-slice simulations summarized in Fig. 2, the optical thickness of the MZIP was deduced as follows. In Fig. 2(a), the simulated intensity inside a slice through the MZIP is shown colour coded, for the case of plane wave-irradiance. The “optimal” thickness for a phase-shifting MZIP would be around  $2.1 \mu\text{m}$ , but due to volume diffraction effects the optical thickness was decided to be only  $0.7 \mu\text{m}$ . Numerically propagated intensity along the optical axis is shown in Fig. 2(b), including higher order foci. We emphasize that the underlying KB beam is several orders of magnitude fainter in intensity. The optimal MZIP focus as simulated for plane wave illumination and perfect layers is shown in Fig. 2(c), promising a focus size of about  $4.4 \text{ nm}$ . In Fig. 2(d), the simulated KB beam in the (KB) defocus position is shown; the red shaded areas depict the approximate position of the active zones. Note that the two-dimensional intensity distribution is rather homogeneous, as it can be approximated by a tensor product of the two curves (horizontal and vertical).

### 3. Fabrication of the multilayer zone plate

In the following we will give more details on the production process by the combination of PLD and FIB.

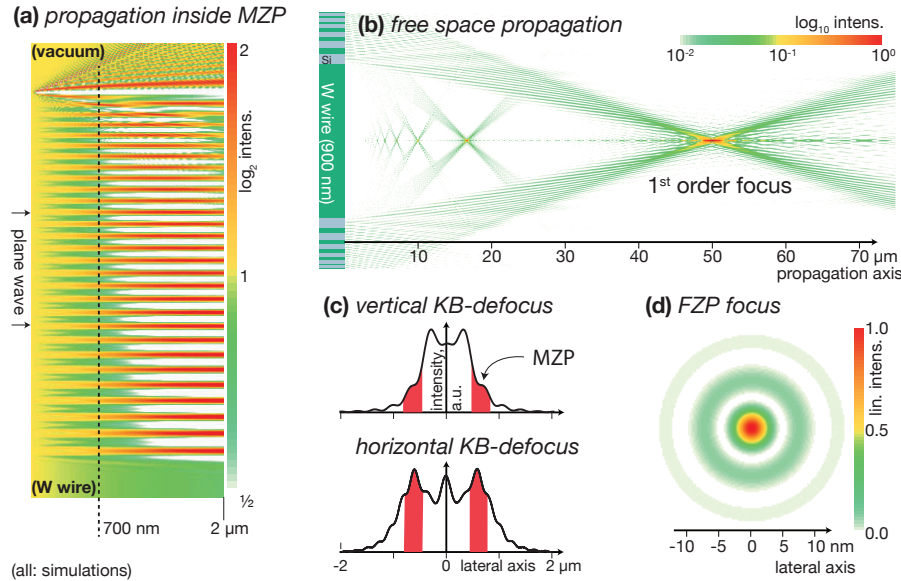


Fig. 2. (a) Multislice-simulation of the field propagation inside the zone plate showing volume effects for long optical lengths of the MZP, that was finally cut to 0.7  $\mu\text{m}$ . (b) Simulated intensity distribution of the MZP-focused field, along the propagation axis and (d) in the focal plane yielding a spot size of 4.4 nm (FWHM). (c) Intensity distribution at the defocus position of the MZP (the positions of the MZP zones are marked)

### 3.1. PLD of the depth graded multilayer on a rotating W wire

In a first step, a couple of W wires were electrolytically thinned down in 2 moles of sodium hydroxide to obtain the desired diameter of about 900 nm over a length of several  $\mu\text{m}$ . From these wires, that one obeying the most uniform diameter of 900 nm with lowest gradient along the wire was selected by scanning electron microscopy measurements (SEM, SEM Nova NanoSEM 650 from FEI).

For the growth of the aperiodic W/Si multilayer onto the rotating W wire, a standard PLD-setup (KrF excimer laser at 248 nm, 30 ns, 10 Hz) was used [26]. Laser fluences of 1.7 J/cm<sup>2</sup> and 3.2 J/cm<sup>2</sup> were chosen, leading to deposition rates of 0.011 nm/pulse and 0.004 nm/pulse for Si and W, respectively. The reduction of the deposition rate during target alteration, resputtering effects at the W/Si interfaces [27] and enhanced resputtering caused by the curvature of the wire had to be compensated for by additional laser pulses and an energy correction algorithm. After multilayer deposition, a W layer of 100 nm thickness was deposited on top to protect the structure during FIB processing.

From the coated wire, a lamellar was prepared using FIB for layer thickness and roughness analysis by TEM (Philips CM30 at 300 kV), refer to Fig. 3(a). The deposited layer thicknesses closely follow the aimed ones as can be seen in Fig. 3(b), in particular for the most relevant outer zones. The crystalline grain structure of the W wire leads to surface roughness and waviness of the innermost zones. However, the PLD growth process is characterized by cumulative smoothening, which is clearly evident and instrumental in this work and most effectively for low spatial frequency roughness components, see Figs. 3(c) and (d). The height deviation functions of individual MZP layers were quantified to investigate the influence of these defects on focusing properties by simulation (see below).

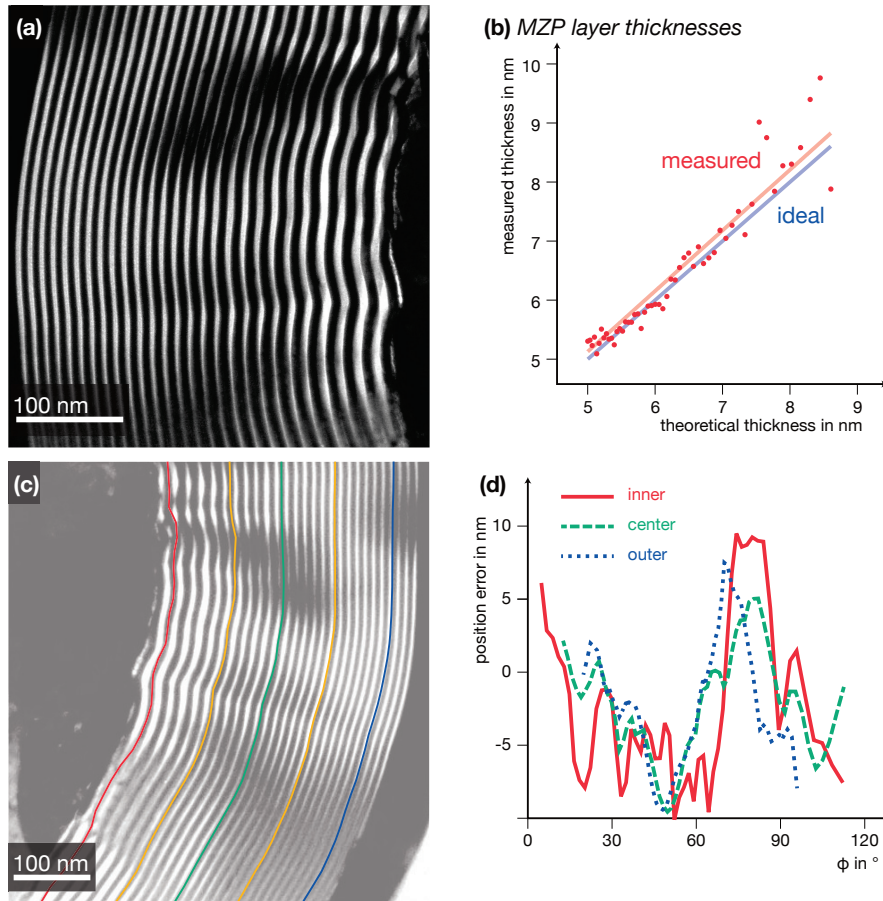


Fig. 3. (a) TEM image of the MZP depicting the multilayer structure as well as a part of the central wire. (b) Comparison of measured and ideal layer thicknesses showing a good agreement, especially for the relevant outer zones. (c) TEM micrograph of a part of the MZP used for the analysis of roughnesses and the smoothing effect. (d) Layer position error as a function of angle for different zone numbers, illustrating the smoothing effect induced by PLD.

### 3.2. FIB processing of the MZP

Within the FIB-facility (Nova NanoLab600, FEI), for further protection an additional layer of Pt was deposited onto the W-coated multilayer by electron beam deposition. Then, the specimen was cut through by a 30 kV  $\text{Ga}^+$ -ion beam (using a current of about 1 nA) close to the region, where the wire had its desired diameter of 900 nm. A piece of the coated wire was attached to a thin W-micromanipulator with electron and ion-beam deposited Pt [Fig. 4(a)] and transferred towards a W tip [Fig. 4(b)] prepared beforehand. Afterwards, the micromanipulator was cut off and drawn back, leaving the coated wire on the W-tip [Fig. 4(c)]. Finally, the lens was shaped and polished by less energetic  $\text{Ga}^+$ -ions (5 kV, ca. 30 pA) down to its final optical thickness of 700 nm. In Fig. 4(d), the finally fabricated MZP sitting on the W tip (ready for the x-ray focusing experiments) is shown from the side view.



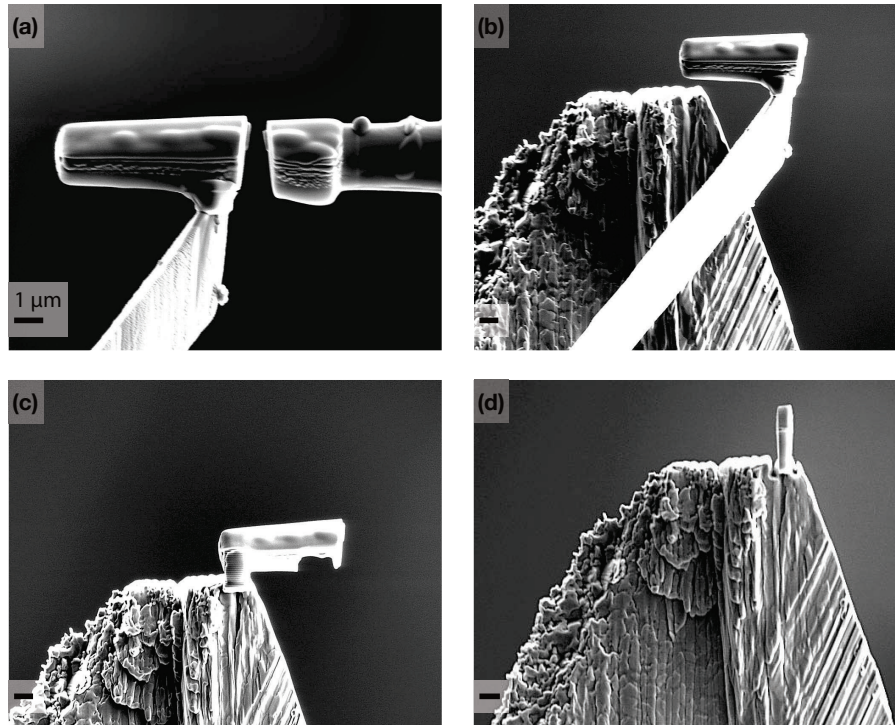


Fig. 4. FIB-fabrication of the MZP: (a) Attaching of the micromanipulator to the coated wire and making a cut off. (b) Placing of the MZP onto a beforehand prepared W tip and attaching by Pt deposition. (c) Removing the micromanipulator from the sample. (d) Thinning out the MZP to the desired optical thickness of 700 nm (side view). See text for details.

## 4. Hard x-ray focusing experiments

### 4.1. Experiment

The synchrotron experiment was carried out at the GINIX setup at the coherence beamline P10 at the synchrotron radiation source PETRA III, DESY, Hamburg. At a wavelength of 0.157 nm (corresponding photon energy: 7.9 keV, Si-111 double-bounce monochromator), the x-ray beam was focused using two total reflection elliptical mirrors in KB geometry to a spot size of about  $400 \text{ nm} \times 200 \text{ nm}$  ( $h \times v$ ). The lens was placed into a defocus position about 2 mm downstream. Slits in front of the KB were closed to obtain full coherence and tailor the beam size to match the MZP diameter: see the simulation of the KB beam respecting the finite source size in Fig. 2(d); shaded in red are the active zones of the MZP. A beamstop was inserted into the primary beam 12.7 mm downstream to protect the detectors. For alignment and to estimate the efficiency, a single-photon counting detector Pilatus 300k (Dectris Inc., Switzerland) was used at a distance of about 5.5 m behind the KB focus. Importantly, the pixel detector image could be recorded without beamstop using appropriate attenuator settings, resulting in a complete data set without missing low spatial frequency modes. A photon flux of about  $10^9$  photons/s was determined outside the zero order leading to an effective efficiency of about 2 % by considering the geometrical beam size of the KB and the acceptance of the MZP [Fig. 1(d)]. This is in line with simulations of MZP-focusing with the measured zone waviness. High-resolution images

were recorded by an sCMOS camera consisting of  $1920 \times 1080$  pixels with pixel size of  $6.5 \mu\text{m}$  positioned at 185 mm behind the KB focus. For the Fourier based iterative image reconstruction scheme detailed below, these detector settings yield a pixel size in the reconstruction plane (focal plane of the MZP) of  $2.3 \text{ nm} \times 4.1 \text{ nm}$ , well suited to investigate ultra-small focal widths. For the autocorrelation analysis, 50 illuminations of each 0.1 s at three horizontal stitching positions were accumulated with the Pilatus detector; the phase-retrieval was carried out with ten averaged illuminations of the sCMOS detector, illuminated for 1 s.

It has to be emphasized that the indirect method using far-field diffraction patterns is robust against vibrations and drift of the MZP and its focus. We cannot rule out that the 5 nm spot jitters on length scales of several or even hundred nanometres; this is for future experiments to measure and optimize.

Simulations have shown that the MZP focus is rather robust against realistic aberrations and potential inhomogeneities of the KB beam.

In case of perfect illumination, Fig. 2(b) and (c) show the simulated intensity distribution of the focused MZP field yielding a spot size of 4.4 nm (FWHM). To measure such a small focus is extremely demanding, in view of the required specifications of knife edge perfection, positioning accuracy, vibration control, and the short focal length. The task would be even more challenging than for the 1D sub-10 nm focus verified by knife edge scanning in [7]. Indeed, knife edge scans only give the intensity distribution along one or two directions, and not in the entire focal plane which is required here. Instead, we chose established phase retrieval algorithms capable of inverting the measured fully coherent far-field intensity pattern. As detailed below, the wave field reconstruction confirms the prediction of a sub-5 nm focus.

The far-field intensity pattern was recorded using (i) a high dynamic range single photon counting pixel detector (Pilatus 300k, Dectris Inc.) for the autocorrelation analysis, and a high-resolution sCMOS detector (Photonic Science) for phase-retrieval, as outlined below. Already the extension of the circular shaped far-field intensity patterns of the MZP – shown in Fig. 5(a) and (d), recorded with different detectors – to large scattering vectors  $q \sim 0.77 \text{ nm}^{-1}$  leads to the conjecture of correspondingly small structures in the focus plane. A first estimation is available from the autocorrelation of the complex-valued focus field  $u_f$  calculated by an inverse Fourier transform of the far-field intensity  $I_d$  shown in Fig. 5(a), given by  $I_d(q_x, q_y) = |U(q_x, q_y)|^2 = \mathcal{F} \int u_f(x', y') u_f^*(x' - x_f, y' - y_f) dx' dy'$  [28]. The result of the autocorrelation with FWHM of 9.2 nm presented in Fig. 5(b) indicates the presence of structures in the focal field intensity distribution of 4.6 nm, assuming a Gaussian distribution. However, the shape of the focused field (or intensity distribution) cannot be inferred from the autocorrelation, for example whether it consists of a single peak or exhibits fringes.

#### 4.2. Iterative Phase Retrieval

Therefore, the complex-valued field in the focal plane was reconstructed based on a three-planes phase-retrieval algorithm [29], as depicted in Fig. 5(c). The optical field is propagated numerically between MZP, focus and detector. A modulus constraint adapting the reconstructed intensities to the measured ones is applied in the detector plane. In the MZP plane we use a support constraint setting the field constant outside the MZP, such that the exit wave is reconstructed within the MZP. After 50 iterations, a far-field pattern – like that in Fig. 5(e) – sufficiently close to the measured intensity pattern of Fig. 5(d) is obtained. For validation and proof of consistency, the reconstructed field in the MZP plane is analysed: The MZP exit wave clearly reveals the expected zones in amplitude and phase, refer to Fig. 5(f-h), in agreement with the measured layer thicknesses in Fig. 4(b). However, the algorithm reconstructs zones within the W wire; this is due to missing data inside the beamstop region, where no constraint is enforced. Note that the contrast of these non-existent zones is weak compared to physical zones.



Next, the two-dimensional focal field is analysed, see Fig. 5(i). The overall intensity distribution in width and location of side minima compares well with the simulation in Fig. 2(c), which assumed perfect plane wave illumination and an ideal MZP structure. Fitting the horizontal and vertical profiles, red points in Fig. 5(j), of the reconstruction to a Gaussian lineshape reveals an unprecedented spot size of  $4.3 \text{ nm} \times 4.7 \text{ nm}$  (FWHM). This 5 nm spot is below the limit conjectured previously to result from the small differences of the x-ray index of refraction  $n$  from unity [30].

#### 4.3. Phase retrieval: Details

Propagation between focus and detector was carried out with a fast Fourier transform (FFT), while a Fresnel near-field propagator  $D_{\pm f}$ , formulated as the convolution form of the Fresnel Kirchhoff integral in paraxial approximation [31], was used to propagate the complex-valued field amplitude  $u_f$  (focus) to the MZP plane,  $u_{zp}$ :

$$u_{zp} = D_{-f} u_f = \mathcal{F}^{-1} \left[ \mathcal{F} u_f \cdot \frac{\exp[ik(-f)]}{i\lambda(-f)} \exp \left[ \frac{ik}{2(-f)} \rho_f^2 \right] \right], \quad (1)$$

where  $\rho_f^2 = x_f^2 + y_f^2$  is the radial coordinate in the focal plane.

The algorithm [29] is initialized in the MZP plane with a homogeneous illumination, followed by near-field propagation to the focal plane  $D_{+f}$ , and a Fourier transformation to the detector (far-field), where a modulus constraint of the measured far-field intensities [Fig. 3(d)] is applied outside the beamstop region  $(x_d, y_d) \notin B$  on the detector. Back in the focal plane, the updated field is

$$u'_f = \begin{cases} \mathcal{F}^{-1} \left[ \sqrt{I_d(x_d, y_d)} \cdot \arg \mathcal{F} u_f \right], & \text{if } (x_d, y_d) \notin B, \\ \mathcal{F}^{-1} \mathcal{F} u_f, & \text{else.} \end{cases} \quad (2)$$

This field is propagated upstream to the MZP plane, where a support constraint is applied outside the MZP's aperture  $A$ , while the field inside  $A$  is accepted,

$$u'_{zp} = \begin{cases} D_{-f} u'_f, & \text{if } (x_{zp}, y_{zp}) \in A \\ 1, & \text{else (KB illumination).} \end{cases} \quad (3)$$

Importantly, no additional constraint is applied in the focal plane.

Some notes on the used constraints: First, approximating the KB-illumination at the MZP plane by a homogeneous amplitude and zero phase is a justified assumption taking into account the fact that the MZP was positioned not in the focus but within the Rayleigh length of the KB-beam. Hence the MZP was fully illuminated due to the slight divergence of the beam and the phase front hitting the optic can still be assumed to be rather flat. Second, using the modulus constraint outside the beamstop region where there is no information about the intensities is equal to letting the algorithm freely construct the zeroth order of the illumination. As a drawback one has no influence on the reconstructed inner region of the MZP which actually should be homogeneous; however, an artificial illumination is reconstructed in the W wire region showing ring artefacts. Nevertheless these artefacts are much smaller in amplitude than the visibly pronounced structured zones.

#### 4.4. The influence of waviness

In view of these unique values, the basic question was whether the small deviations in layer thickness or the roughness (quantified in Fig. 3) of the MZP layers with an amplitude exceeding

the outermost zone width should not have a detrimental effect on the spot size. Simulating the measured values of the zone radii without roughness yields a focus size of  $4.3 \text{ nm} \times 4.9 \text{ nm}$  (FWHM).

To investigate the influence of wire roughness on the focusing properties, in particular focal size and efficiency, the wavefield behind distorted zoneplates has been simulated. The ideal experimental parameters (zone numbers and width, tungsten and silicon layers, optical depth  $z = 700 \text{ nm}$ , wavelength  $\lambda = 0.157 \text{ nm}$ ) were adapted to the experimental parameters. The roughness parameters used in the simulation have been chosen close to the experimental values and beyond. Conformal layer fluctuations with constant radial wavenumber (harmonic), roughly matching the experimental case, were added in the simulations to model low-frequency deviations, that remain in spite of the smoothing PLD process. For this, the start structure was deformed by a conformal height fluctuation  $\varepsilon(\varphi)$  as a function of the polar angle  $\varphi$ , with zone radii

$$r_n = \sqrt{(n\lambda/2)^2 + n\lambda f} + \varepsilon(\varphi). \quad (4)$$

To dissect the effects of the angular harmonic  $m$  (or correspondingly the fluctuation wavelength) and the fluctuation amplitude  $A_m$ , a simple sinusoidal height deviation was chosen  $\varepsilon(\varphi) = A_m \cdot \sin(m\varphi)$  varying both parameters to model different conformal roughness components. As a result, we find that focusing properties are surprisingly robust with respect to conformal height fluctuations, which is the dominating type of defect in the present MZP fabrication process. These conformal layer fluctuations (preserving the zone thickness) only change the focusing efficiency (experimentally determined to be about 2 %) similar to a Debye-Waller like factor, but not the spot size. Compared to the ideal MZP,  $\pm 7 \text{ nm}$  height fluctuations – if assumed to be conformal – still show more than 10% efficiency, and a width which increases from 4.4 nm to 4.5 nm, i.e. essentially unaltered.

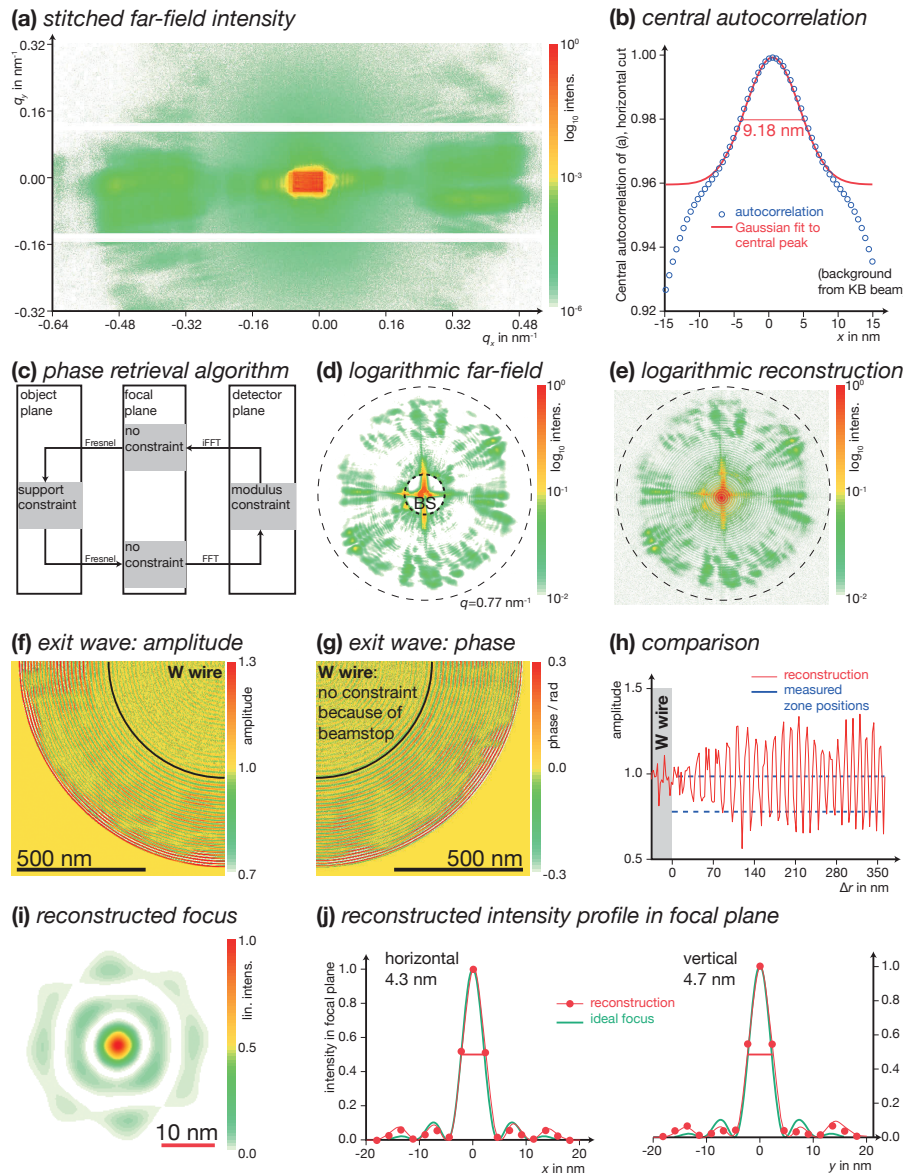


Fig. 5. Analysis of the measured far-field intensity yielding a spot size below 5 nm.

(a) Stitched far-field intensity pattern obtained by a high dynamic range pixel detector (Pilatus 300k). (b), Central autocorrelation (of (a)) of width 9.2 nm, indicating structures of 4.6 nm in the focal field. (c), Illustration of the three-planes phase-retrieval algorithm. (d), Measured far-field intensity obtained with the sCMOS detector. (e), Reconstruction of the far-field intensity obtained via the phase-retrieval algorithm, in good agreement to the measured data (d). (f-h), Reconstructed field showing the amplitude (f) and phase (g) of the exit wave in the MZP plane revealing the measured zones (h); note that virtual zones inside the W wire are not interdicted due to the far-field beamstop. (i), Reconstruction of the two-dimensional focus field, comparing well with the simulation in Fig. 2(d). (j), Line profiles of the horizontal and vertical focus intensities yielding a spot size of  $4.3 \text{ nm} \times 4.7 \text{ nm}$  (FWHM of Gaussian fit, red line).

The  $k$  dependence was found to be very weak. Using a smoother wire for deposition, for example by replacing the poly-crystalline W by amorphous glass/quartz, an achievable amplitude of 2 nm would yield an efficiency which is 60 % of the ideal case. The main results are illustrated in Fig. 6.

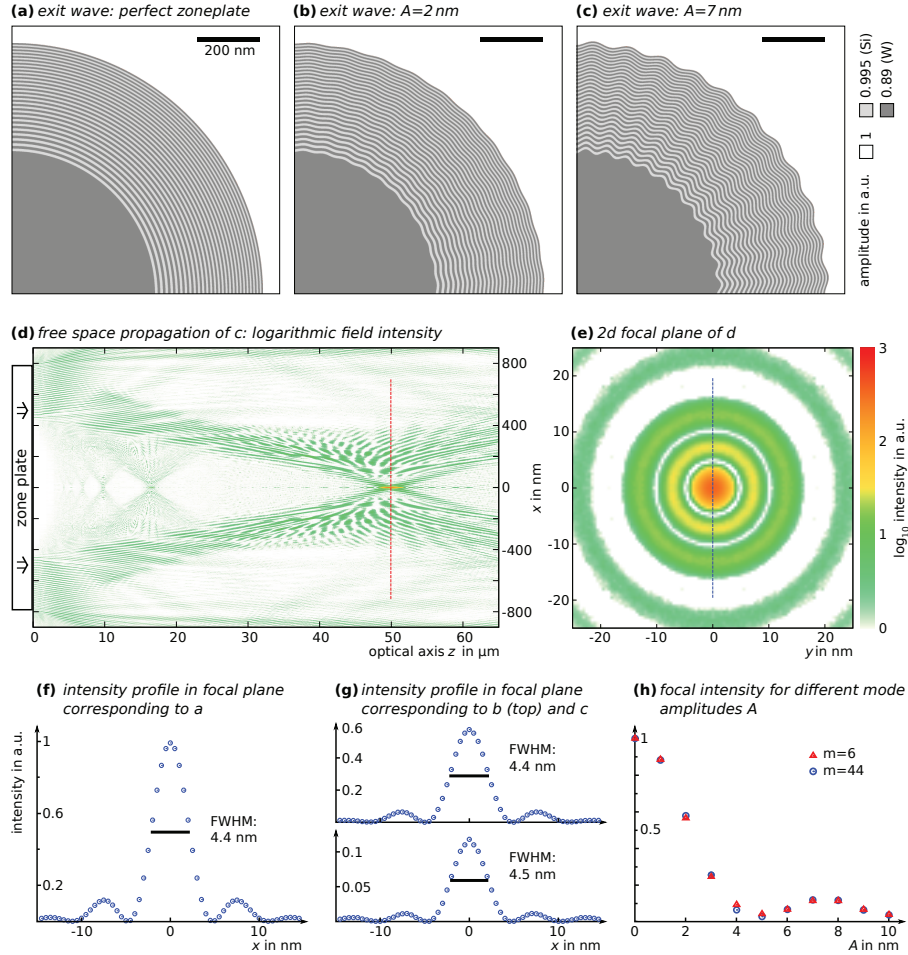


Fig. 6. Simulations of the focusing properties of distorted MZPs with conformal height fluctuations. Corresponding to (a) the ideal case, (b)  $A_{44} = 2$  nm, and (c)  $A_{44} = 7$  nm, for constant  $m = 44$ . The images represent the resulting exit waves, i.e. the wavefield directly behind the MZP. As a result of the distorted exit wave, the focal length  $f$  can slightly deviate from the ideal case. Therefore, the exit waves were propagated to a set of planes around  $f$  using the Fresnel propagator to identify the plane with the highest intensity, see (d) for the case of  $A_{44} = 7$  nm, and (e) for the resulting focal intensity distribution. The one-dimensional intensity profiles through the focus shown in (f), (g) and (h), for the cases of (a), (b), and (c), respectively show that the width remains almost unaltered, while the intensity increases, as detailed for a wider range of  $A_m$  in (h).

Two important conclusions can be drawn: First, the common notion that rms-roughness has to be smaller than the outermost zone width  $dr$  can be relaxed, if the wavenumber of the height fluctuation is sufficiently small and roughness is conformal which is the case for the present PLD growth regime. Second, an efficiency gain of about an order of magnitude can be antici-

pated by replacing the multi-grain W wire by a suitable amorphous wire (e.g. a thinned glass fibre).

## 5. Conclusion

In summary we have shown that sub – 5 nm hard x-ray point focusing was reached in a compound optics by the combination of a high gain elliptical KB-mirror system for pre-focusing and a high resolution MZP positioned nearby the focal plane of the KB mirror. The MZP was fabricated by PLD and FIB leading to an outermost zone width of about 5 nm. In view of applications, MZPs fabricated according to the presented concept can easily be placed as a high resolution option into the micrometre-focus of current hard x-ray endstations enabling new opportunities such as high-resolution scanning x-ray transmission microscopy.

## Acknowledgments

We thank Volker Radisch for support using the FIB, and Michael Sprung and the entire *P10/HASYLAB/DESY* team for excellent working conditions. We acknowledge financial support by the Deutsche Forschungsgemeinschaft through SFB 755 *Nanoscale Photonic Imaging* and the German Ministry of Education and Research under Grants No. 05KS7MGA and 05K10MGA.